Beyond MACs: Deployment-Constrained Design Space Exploration for Tensorized Neural Networks

Jinsong Zhang[1,*], Minghe Li[1,2,*], Jiayi Tian[1], Jinming Lu[1,†], Zheng Zhang[1,†]
Email: {jinsongzhang, jiayi_tian}@ucsb.edu; zhengzhang@ece.ucsb.edu
mli247@jh.edu; jinmingmaster@gmail.com
[1]Department of Electrical and Computer Engineering, University of California, Santa Barbara, CA, USA
[2]Department of Electrical and Computer Engineering, Johns Hopkins University, Baltimore, MD, USA

arXiv:2511.17971v3 [cs.AR] 2 Nov 2026

***Abstract*—Tensor-train (TT) compression reduces neural-network parameters, but the latency of a tensorized layer is set by its contraction order and its mapping onto hardware: a contraction path with fewer multiply–accumulate operations (MACs) is not necessarily faster on a systolic array. We present a deployment-constrained, latency-guided design space exploration (DSE) framework for fixed-rank tensorized neural networks (TNNs) under a fixed processing-element (PE) budget. Using MAC-guided path pruning, it evaluates feasible combinations of contraction paths, three PE-array partitions, and input-, output-, and weight-stationary dataflows. By minimizing the sum of inference and training latency estimates, it selects a single physical PE partition shared across layers and both modes, while allowing layer- and mode-specific paths and dataflows. On ResNet-18 and ViT-Ti/4, 25%–50% of the layers select a path other than the minimum-MAC one, the best dataflow varies across layers and models, and on a representative ViT layer the latency-selected candidate reduces simulated latency by 23.5% relative to the minimum-MAC candidate. Deployed on a Xilinx VU9P FPGA accelerator that supports both inference and training, the complete TT+INT8 system achieves 3.28×–4.00× inference and 3.42×–3.85× training speedups over dense implementations with the same PE budget.**

***Index Terms*—Tensorized neural networks, tensor contraction, FPGA, dataflow mapping, design space exploration**

I. Introduction

Deep neural networks (DNNs) have advanced image classification [1] and object detection [2], but their computation and storage demands challenge edge hardware. Tensor decomposition [3], [4], and tensor-train (TT) decomposition in particular, represents neural-network weights with compact low-rank cores, reducing the storage cost of edge deployment [5]–[7]. Related low-rank and tensor-compression work covers convolutional, recurrent, and large language models as well as rank selection [8]–[15]. Quantization [16]–[18], sparsity [19]–[22], memory-efficient on-device learning [23], and quantization- or hardware-aware compression [24], [25] further reduce deployment cost. However, fewer parameters or multiply–accumulate operations (MACs) do not necessarily imply lower hardware latency. A TT layer executes a sequence of contractions, and their order changes intermediate matrix shapes, processing-element (PE) utilization, and operand reuse. In Fig. 1, a latency-selected configuration for a ViT layer uses approximately 0.24% more MACs than the minimum-MAC candidate yet reduces simulated latency by 23.5%.

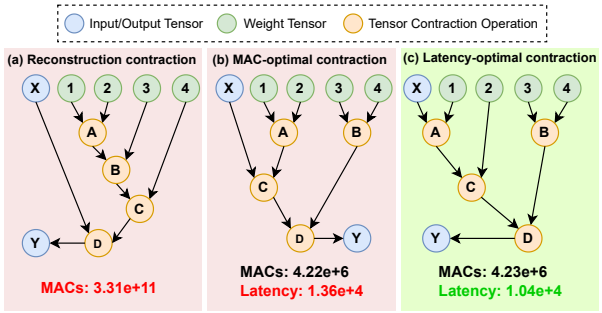


Fig. 1. Contraction paths of a TT layer in ViT-Ti/4 (CIFAR-10): (a) reconstruction-based, (b) minimum-MAC (4.22×10^6 MACs, 1.36×10^4 cycles), and (c) latency-selected (4.23×10^6 MACs, 1.04×10^4 cycles).

Mapping decisions have different deployment granularity. Contraction paths and input-, output-, or weight-stationary (IS/OS/WS) dataflows can vary by layer and execution mode, whereas the physical PE-array partition remains fixed in the FPGA. Independently choosing each layer's preferred partition is therefore not deployable; fixing all mappings instead ignores heterogeneous contraction shapes and opportunities for parallel branches.

Relation to prior work. Prior studies have demonstrated the benefits of hardware-aware tensor decomposition and contraction mapping. HEAT explores tensorization shape and rank alongside contraction paths and fused Einsum mapping [26]. TetriX combines mapping-aware sequence selection with flexible hardware and tensor-layout management [27]. FETTA searches contraction sequences and employs reconfigurable engines for TNN training [28], while related FPGA work uses bidirectional TT contractions [29] and ultra-low-memory tensorized training [30]. Systolic arrays [31] with weight-, output-, or input-stationary dataflows [32], [33] are widely used for DNN acceleration, and tools such as Timeloop, MAESTRO, and SCALE-Sim explore their mappings [34]–[36]. These tools take the operator shapes as given, whereas in a TT layer the contraction order itself determines these shapes. Complementary FPGA training accelerators investigate data

*Equal contribution. †Corresponding authors.

reshaping and low-precision arithmetic [37], [38]. We focus on a deployment-level optimization challenge: a distinct deployment constraint where *one fixed PE partition must serve all layers and both inference and training of a given fixed-rank TNN*, while paths and dataflows remain layer- and mode-specific.

To address this deployment constraint, we develop a latency-guided design space exploration (DSE) framework that jointly considers contraction paths, PE-array partitions, and stationary dataflows. For each candidate partition, layer-specific inference and training latency estimates are minimized and summed to choose one shared partition. The selected mappings run on an FPGA GEMM and streaming TT engine that supports both inference and training.

Our contributions are:

- **Deployment-constrained DSE.** Under a fixed PE budget, we select one partition for inference and training jointly, with layer- and mode-specific paths and dataflows, minimizing modeled latency over retained feasible candidates.
- **Hardware-sensitive mapping analysis.** In 25%–50% of evaluated layers, the selected path is not minimum-MAC; one ViT layer exhibits 23.5% lower simulated latency. Dataflow and split-array preferences also vary across workloads.
- **FPGA validation.** A VU9P implementation supports CNN and ViT inference and training and achieves 3.28×–4.00× inference and 3.42×–3.85× training speedups over matched INT8 dense implementations.

II. Background: Tensorized Layers

A d-way tensor $\mathcal{A} \in \mathbb{R}^{n_1 \times \cdots \times n_d}$ has d modes of sizes $n_1, \ldots, n_d$ [3]. In a tensor graph (Fig. 2(a)–(b)), a d-way tensor is a node with d edges, so a matrix is a node with two edges. Contracting mode s of $\mathcal{A}$ with mode t of $\mathcal{B} \in \mathbb{R}^{m_1 \times \cdots \times m_q}$ ($n_s = m_t$) is written as $\mathcal{C} = \mathcal{A} \times_s^t \mathcal{B}$, which sums over the shared mode; $\mathcal{C}$ keeps the remaining modes of $\mathcal{A}$ followed by those of $\mathcal{B}$. Fig. 2(c)–(d) shows contractions of 2-way and 3-way tensors, the former being a matrix multiplication; the free (unconnected) edges give the modes of the result. After reshaping, every contraction is executed as a GEMM, and different contraction orders produce different intermediate shapes and MAC counts.

TT linear layer. For $\mathbf{W} \in \mathbb{R}^{M \times N}$ with $M = \prod_{i=1}^{d} m_i$ and $N = \prod_{i=1}^{d} n_i$, $\mathbf{W}$ is reshaped into a $2d$-way tensor $\mathcal{W}$ of size $m_1 \times \cdots \times m_d \times n_1 \times \cdots \times n_d$ and represented by $2d$ TT cores [6] as $\mathcal{W} = \mathcal{G}_1 \times_3^1 \mathcal{G}_2 \times_3^1 \cdots \times_3^1 \mathcal{G}_{2d}$, where $\mathcal{G}_k \in \mathbb{R}^{r_{k-1} \times q_k \times r_k}$, $q_k = m_k$ for $k \le d$, $q_k = n_{k-d}$ otherwise, and $r_0 = r_{2d} = 1$. The cores hold $\sum_k r_{k-1} q_k r_k$ parameters instead of MN. The forward pass maps $\mathcal{X} \in \mathbb{R}^{n_1 \times \cdots \times n_d}$ to $\mathcal{Y} \in \mathbb{R}^{m_1 \times \cdots \times m_d}$. Let $\mathbf{i} = (i_1, \ldots, i_d)$ and $\mathbf{j} = (j_1, \ldots, j_d)$. Then

$$\mathcal{Y}[\mathbf{i}] = \sum_{\mathbf{j}} \Big(\prod_{k=1}^{d} \mathcal{G}_k[i_k] \Big) \Big(\prod_{k=1}^{d} \mathcal{G}_{d+k}[j_k] \Big) \mathcal{X}[\mathbf{j}], \tag{1}$$

where $\mathcal{G}_k[i]$ is the i-th $r_{k-1} \times r_k$ slice of $\mathcal{G}_k$ (Fig. 2(e)). The cores and input admit multiple valid contraction orders that preserve the intended tensor-network contraction.

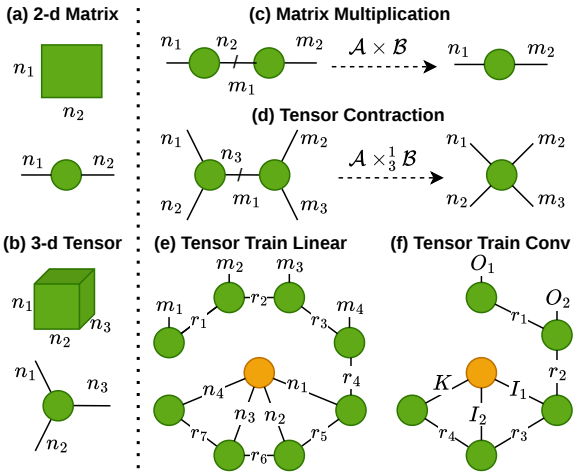


Fig. 2. Tensor graphs: (a) matrix, (b) tensor, (c) matrix multiplication, (d) contraction, (e) TT linear layer, and (f) TT convolution layer.

TT convolution layer. For $\mathcal{W} \in \mathbb{R}^{C_{out} \times C_{in} \times K_h \times K_w}$, we factor $C_{out} = O_1 O_2$ and $C_{in} = I_1 I_2$ and set $K = K_h K_w$, giving five cores with mode sizes (O_1, O_2, I_1, I_2, K). This reduces the parameter count from $O(C_{out} C_{in} K)$ to $O(r^2(C_{out} + C_{in}) + rK)$. For the unfolded input $\mathcal{X}_{\text{unf}} \in \mathbb{R}^{I_1 \times I_2 \times K \times N_{\text{p}}}$ with N_{p} spatial patches indexed by ν, let $\mathbf{o} = (o_1, o_2)$, $\mathbf{u} = (i_1, i_2, k)$, and $\mathbf{s} = (o_1, o_2, i_1, i_2, k)$. Then

$$\mathcal{Y}_{\text{col}}[\mathbf{o}, \nu] = \sum_{\mathbf{u}} \Big(\prod_{t=1}^{5} \mathcal{G}_t[s_t] \Big) \mathcal{X}_{\text{unf}}[\mathbf{u}, \nu], \tag{2}$$

so the input interacts with the input-side cores $\mathcal{G}_3$–$\mathcal{G}_5$, and the output-side cores $\mathcal{G}_1, \mathcal{G}_2$ generate the output channels (Fig. 2(f)). In training, the backward pass adds contractions for the input and core gradients, which are also free to reorder.

III. Deployment-Constrained DSE

Given a fixed-rank TNN and a fixed PE budget, the proposed DSE framework considers three physical array partitions (Fig. 3). A partition is selected once per model and is shared by inference and training; the executed contraction paths and dataflows may depend on both the layer and the execution mode. The training accelerator extends the inference datapath with backward and weight-update support, so both modes execute on the same PE-array organization and the partition must serve both.

A. Problem Formulation

Let $\mathcal{Q} = \{\text{inf}, \text{train}\}$ denote the two execution modes and $l = 1, \ldots, L$ index the model layers. The TT ranks, model weights, and INT8 arithmetic are fixed before the mapping search. For layer l and mode q, let $\mathcal{P}_l^q$ denote at most K candidate contraction paths, and let $\mathcal{D} = \{\text{IS}, \text{OS}, \text{WS}\}$ denote the available stationary dataflows. The global partition h is chosen from $\mathcal{H} = \{1{\times}1, 1{\times}2, 2{\times}1\}$; the last two configurations split the same PE budget into two equal subarrays. The feasible path/dataflow pairs under h form $\mathcal{F}_l^q(h) \subseteq \mathcal{P}_l^q \times \mathcal{D}$. Denote

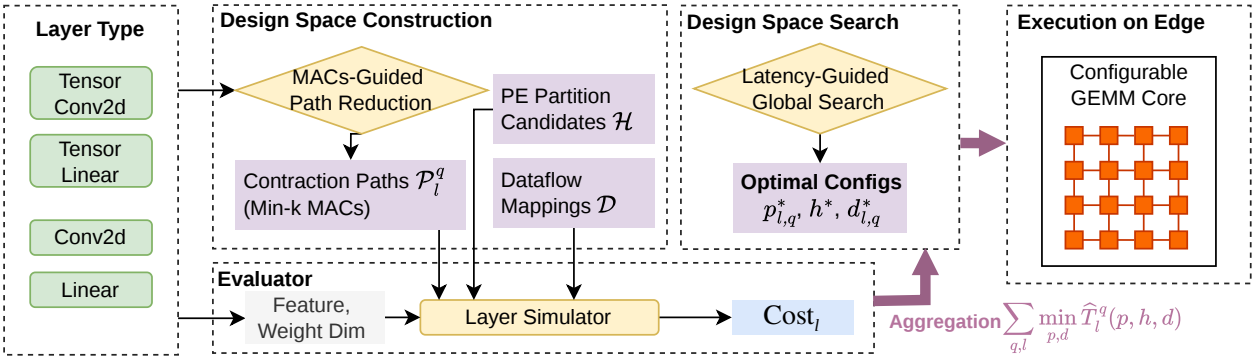


Fig. 3. Deployment-constrained DSE flow. MAC-guided pruning generates candidate paths, and a simulator evaluates feasible path/partition/dataflow combinations. Layer-level inference and training latency estimates are aggregated for each partition; the partition with the lowest combined model latency is fixed for deployment. Paths and dataflows can differ by layer and execution mode.

the simulated latency of a feasible mapping by $\widehat{T}_l^q(p,h,d)$. We select

$$h^* = \arg\min_{h\in\mathcal{H}} \sum_{q\in\mathcal{Q}} \sum_{l=1}^{L} \min_{(p,d)\in\mathcal{F}_l^q(h)} \widehat{T}_l^q(p,h,d). \tag{3}$$

For each candidate h, the inner minimizations select the path and dataflow for each layer and mode; their inference and training costs are summed with equal weights to select one shared h^*. After selecting h^*, each $(p_{l,q}^*, d_{l,q}^*)$ is the corresponding inner minimizer. A partition for which any required $\mathcal{F}_l^q(h)$ is empty is infeasible. The formulation assumes additive layer costs and does not model cross-layer overlap or inter-layer transfer beyond the simulator estimates.

B. Candidate Paths and Search

MAC-guided pruning. Similar to contraction-order search for general tensor expressions [39], a depth-first exploration builds contraction orders, eliminates equivalent candidates and high-MAC branches, and retains up to K low-MAC paths per layer and mode. MAC count is used only to prune the space; the final choice is made by simulated latency. Independent contraction branches can be mapped concurrently to the two fixed subarrays in a feasible split configuration [29].

Latency-based selection. SCALE-Sim v3 [36] evaluates each feasible (p,h,d) for the corresponding layer and execution mode. For each h, the minimum estimated latency is found independently within every (l,q) group and then added across layers and modes; the lowest combined total selects h^*. With at most K paths, three partitions, and three dataflows, at most $2|\mathcal{H}||\mathcal{D}|KL = 18KL$ mode/layer/configuration evaluations are required, and the selection is exact over the retained candidates.

C. Hardware Realization

The selected mappings are executed on a configurable FPGA accelerator written in C++ HLS, which serves to validate the search results in hardware. A parameterizable $M_{\mathrm{PE}} \times N_{\mathrm{PE}}$ INT8 systolic GEMM engine, whose tiling unit maps the irregular (M,K,N) GEMMs of TT contractions into $\langle T_M, T_N, T_K \rangle$ tiles, is driven by a streaming TT contraction kernel that issues each layer's contractions in the selected order. The array is organized as one array or as two $M_{\mathrm{PE}} \times \frac{N_{\mathrm{PE}}}{2}$ or $\frac{M_{\mathrm{PE}}}{2} \times N_{\mathrm{PE}}$ subarrays according to h^*, which stays fixed during execution; independent branches are assigned to the two subarrays when feasible, and dependent contractions are scheduled after their inputs become available. The engine uses routing multiplexers, configurable on-chip buffer roles, and PE control registers to select IS/OS/WS dataflows for the scheduled workload without changing the physical partition or regenerating the bitstream. Forward contractions and the backward computations of the evaluated TT linear and convolution layers are scheduled on the same engine, which supports both inference and training.

TABLE I
TOP-1 ACCURACY AND PARAMETER COMPRESSION.

Model / Dataset	Original (%)	TT+INT8 (%)	Params↓
ResNet-18 / CIFAR-10	93.33	92.62	38.72×
ResNet-18 / Tiny ImageNet	50.81	48.69	35.82×
ViT-Ti/4 / CIFAR-10	81.84	79.10	12.17×

IV. Experimental Results

A. Setup

We evaluate ResNet-18 on CIFAR-10 and Tiny ImageNet and ViT-Ti/4 on CIFAR-10, for inference and training. TT ranks and INT8 precision are fixed before the search. As Table I shows, the TT+INT8 models have 38.72×, 35.82×, and 12.17× fewer parameters than the original models, at accuracy reductions of 0.71, 2.12, and 2.74 percentage points. The search keeps the TT ranks and the quantized model fixed, so accuracy is determined solely by the evaluated TT+INT8 representations.

The simulator models 32×32 PEs with 3072 KB input/weight and 1024 KB output SRAM; the 1×2 and 2×1 partitions thus correspond to two 32×16 and two 16×32 subarrays, respectively, and up to $K = 6$ paths are retained

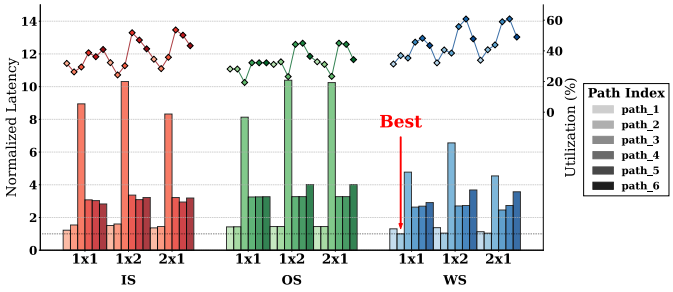


Fig. 4. Layer-level simulated latency of the retained contraction paths under three PE partitions and IS/OS/WS dataflows.

TABLE II
LAYER-LEVEL MAPPING STATISTICS. *Split pref.*: LAYERS WHOSE FASTEST CONFIGURATION USES A SPLIT ARRAY IF EACH LAYER COULD CHOOSE ITS OWN PARTITION. *Non-min-MAC*: LAYERS WHOSE SELECTED PATH IS NOT THE MINIMUM-MAC ONE. LAST COLUMN: SHARE OF LAYERS USING EACH DATAFLOW.

Bench.	Mode	Split pref.	Non-min-MAC	IS / OS / WS (%)
RN18-C10	Inf.	100%	25%	25 / 75 / 0
	Train	100%	25%	43.8 / 56.2 / 0
RN18-TIN	Inf.	100%	25%	50 / 50 / 0
	Train	100%	25%	62.5 / 37.5 / 0
ViT-C10	Inf.	50%	50%	0 / 0 / 100
	Train	50%	50%	0 / 66.7 / 33.3

TABLE III
FPGA RESULTS ON VU9P (200 MHZ, SAME TOTAL PE COUNT).

Bench.	Method	BRAM	FF	LUT	Power (W)	Lat. (ms)
Inference						
RN18-C10	Dense	892	342k	318k	14.2	6.40
	TT+DSE	956	408k	390k	11.8	1.60 (4.00×)
RN18-TIN	Dense	1125	415k	388k	15.8	19.20
	TT+DSE	922	475k	452k	12.5	4.90 (3.92×)
ViT-C10	Dense	1085	368k	345k	15.1	8.69
	TT+DSE	1010	422k	396k	12.7	2.65 (3.28×)
Training						
RN18-C10	Dense	1580	452k	428k	25.8	20.40
	TT+DSE	1482	524k	525k	21.2	5.30 (3.85×)
RN18-TIN	Dense	1725	540k	510k	26.1	61.50
	TT+DSE	1428	595k	565k	22.8	16.10 (3.82×)
ViT-C10	Dense	1620	481k	458k	26.7	24.30
	TT+DSE	1515	531k	534k	22.5	7.11 (3.42×)

per layer and mode. The accelerator is implemented with Vitis HLS 2024.2 on a Xilinx VU9P at 200 MHz. The *Dense* baseline uses INT8 arithmetic under the same FPGA and PE-budget setting; *TT+DSE* executes the TT+INT8 representation with the joint-mode, fixed-partition mapping.

B. Layer-Level Mapping Analysis

Layer-level sensitivity. Fig. 4 reports the simulated latency and utilization of retained paths under the three partitions and IS/OS/WS mappings. Paths are indexed in increasing MAC order, so path_1 is the minimum-MAC candidate. For this layer, simulated latency spans more than $10\times$ across the retained configurations, and the fastest one uses path_2 with WS on the single array, rather than path_1. Different contraction shapes exhibit different utilization, so lower MAC count alone need not imply lower execution time, which motivates selecting mappings by simulated latency.

Contraction paths. Table II shows that 25% of ResNet-18 layers and 50% of ViT-Ti/4 layers use a path other than the minimum-MAC candidate under the selected mapping. For the ViT layer in Fig. 1, the latency-selected path reduces the estimated cycle count from 1.36×10^4 to 1.04×10^4 (23.5%) despite slightly more MACs.

Dataflows. ResNet-18 mappings alternate between IS and OS, whereas the ViT-Ti/4 inference mappings select WS and its training mappings predominantly select OS. No single preselected dataflow therefore fits every contraction, which motivates per-layer dataflow selection.

Shared partition. The split-preference column reports what each layer would prefer if allowed to choose its own physical partition: 100% of evaluated ResNet-18 layers and 50% of ViT-Ti/4 layers prefer a split. The global search resolves these competing layer-level preferences under a shared partition constraint; Eq. (3) instead selects one partition by combining inference and training costs, while retaining the mode-specific path and dataflow choices reflected in the other columns. The selected partition is $h^* = 2 \times 1$ (two 16×32 subarrays) for ResNet-18 and $h^* = 1 \times 2$ (two 32×16 subarrays) for ViT-Ti/4; although only half of the ViT-Ti/4 layers prefer a split, the combined inference and training cost still favors one.

C. FPGA Results

Compared with Dense, TT+DSE reduces latency by 3.28×–4.00× for inference and 3.42×–3.85× for training (Table III), and power by 15.9%–20.9% and 12.6%–17.8%. These ratios reflect TT compression together with the selected mapping. The added control and dataflow flexibility costs 11%–23% more LUTs. BRAM changes by only -18.0% to $+7.2\%$, far less than the parameter reduction, because BRAM also holds activations, intermediate tensors, and tile buffers, not only weights. For each model, the inference and training builds use the same partition h^*; the training build additionally contains the backward and weight-update logic with its buffers, which accounts for its higher BRAM, FF, and LUT usage, a trend also seen in the Dense baselines.

V. CONCLUSION

We presented a deployment-constrained, latency-guided DSE framework that selects a single physical PE partition shared by all layers and both inference and training, while choosing contraction paths and stationary dataflows per layer and mode. The layer-level results expose mismatches between MAC count and simulated latency, while the VU9P implementation demonstrates 3.28×–4.00× inference and 3.42×–3.85× training speedups over the INT8 dense baseline under the same PE budget. Future work will extend the deployment-constrained exploration to adaptive tensor ranks and larger-scale neural networks.

REFERENCES

[1] K. He, X. Zhang, S. Ren, and J. Sun, "Deep residual learning for image recognition," in *Proceedings of the IEEE Conference on Computer Vision and Pattern Recognition (CVPR)*, 2016, pp. 770–778.

[2] C. Szegedy, A. Toshev, and D. Erhan, "Deep neural networks for object detection," in *Advances in Neural Information Processing Systems (NeurIPS)*, vol. 26, 2013.

[3] T. G. Kolda and B. W. Bader, "Tensor decompositions and applications," *SIAM Review*, vol. 51, no. 3, pp. 455–500, 2009.

[4] N. D. Sidiropoulos, L. De Lathauwer, X. Fu, K. Huang, E. E. Papalexakis, and C. Faloutsos, "Tensor decomposition for signal processing and machine learning," *IEEE Transactions on Signal Processing*, vol. 65, no. 13, pp. 3551–3582, 2017.

[5] A. Novikov, D. Podoprikhin, A. Osokin, and D. P. Vetrov, "Tensorizing neural networks," in *Advances in Neural Information Processing Systems (NeurIPS)*, vol. 28, 2015.

[6] I. V. Oseledets, "Tensor-train decomposition," *SIAM Journal on Scientific Computing*, vol. 33, no. 5, pp. 2295–2317, 2011.

[7] Z. Yang, Z. Liu, S. Choudhary, X. Xie, C. Gao, S. Kunzmann, and Z. Zhang, "CoMERA: Computing- and memory-efficient training via rank-adaptive tensor optimization," in *Advances in Neural Information Processing Systems (NeurIPS)*, vol. 37, 2024, pp. 77 200–77 225.

[8] Y.-D. Kim, E. Park, S. Yoo, T. Choi, L. Yang, and D. Shin, "Compression of deep convolutional neural networks for fast and low power mobile applications," in *International Conference on Learning Representations (ICLR)*, 2016.

[9] A. Tjandra, S. Sakti, and S. Nakamura, "Compressing recurrent neural network with tensor train," in *International Joint Conference on Neural Networks (IJCNN)*. IEEE, 2017, pp. 4451–4458.

[10] M. Yin, S. Liao, X.-Y. Liu, X. Wang, and B. Yuan, "Towards extremely compact RNNs for video recognition with fully decomposed hierarchical Tucker structure," in *Proceedings of the IEEE/CVF Conference on Computer Vision and Pattern Recognition (CVPR)*, 2021, pp. 12 085–12 094.

[11] M. Yin, Y. Sui, S. Liao, and B. Yuan, "Towards efficient tensor decomposition-based DNN model compression with optimization framework," in *Proceedings of the IEEE/CVF Conference on Computer Vision and Pattern Recognition (CVPR)*, 2021, pp. 10 674–10 683.

[12] M. Yin, Y. Sui, W. Yang, X. Zang, Y. Gong, and B. Yuan, "HODEC: Towards efficient high-order decomposed convolutional neural networks," in *Proceedings of the IEEE/CVF Conference on Computer Vision and Pattern Recognition (CVPR)*, 2022, pp. 12 299–12 308.

[13] J. Tian, R. Solgi, J. Lu, Y. Yang, H. Li, and Z. Zhang, "FLAT-LLM: Fine-grained low-rank activation space transformation for large language model compression," *arXiv preprint arXiv:2505.23966*, 2025.

[14] C. Hawkins and Z. Zhang, "Bayesian tensorized neural networks with automatic rank selection," *Neurocomputing*, vol. 453, pp. 172–180, 2021.

[15] C. Hawkins, X. Liu, and Z. Zhang, "Towards compact neural networks via end-to-end training: A Bayesian tensor approach with automatic rank determination," *SIAM Journal on Mathematics of Data Science*, vol. 4, no. 1, pp. 46–71, 2022.

[16] M. Wang, S. Rasoulinezhad, P. H. Leong, and H. K.-H. So, "NITI: Training integer neural networks using integer-only arithmetic," *IEEE Transactions on Parallel and Distributed Systems*, vol. 33, no. 11, pp. 3249–3261, 2022.

[17] J. Lu, C. Ni, and Z. Wang, "ETA: An efficient training accelerator for DNNs based on hardware-algorithm co-optimization," *IEEE Transactions on Neural Networks and Learning Systems*, vol. 34, no. 10, pp. 7660–7674, 2023.

[18] D. Xu, M. Xu, Q. Wang, S. Wang, Y. Ma, K. Huang, G. Huang, X. Jin, and X. Liu, "Mandheling: Mixed-precision on-device DNN training with DSP offloading," in *Proceedings of the 28th Annual International Conference on Mobile Computing and Networking (MobiCom)*, 2022, pp. 214–227.

[19] H. Wang, W. Liu, T. Xu, J. Lin, and Z. Wang, "A low-latency sparse-Winograd accelerator for convolutional neural networks," in *IEEE International Conference on Acoustics, Speech and Signal Processing (ICASSP)*. IEEE, 2019, pp. 1448–1452.

[20] J. Lu, J. Huang, and Z. Wang, "THETA: A high-efficiency training accelerator for DNNs with triple-side sparsity exploration," *IEEE Transactions on Very Large Scale Integration (VLSI) Systems*, vol. 30, no. 8, pp. 1034–1046, 2022.

[21] C. Fang, W. Sun, A. Zhou, and Z. Wang, "Efficient N:M sparse DNN training using algorithm, architecture, and dataflow co-design," *IEEE Transactions on Computer-Aided Design of Integrated Circuits and Systems*, vol. 43, no. 2, pp. 506–519, 2024.

[22] ——, "CEST: Computation-efficient N:M sparse training for deep neural networks," in *Design, Automation & Test in Europe Conference & Exhibition (DATE)*. IEEE, 2023, pp. 1–2.

[23] Q. Wang, M. Xu, C. Jin, X. Dong, J. Yuan, X. Jin, G. Huang, Y. Liu, and X. Liu, "Melon: Breaking the memory wall for resource-efficient on-device machine learning," in *Proceedings of the 20th Annual International Conference on Mobile Systems, Applications and Services (MobiSys)*, 2022, pp. 450–463.

[24] Z. Yang, S. Choudhary, S. Kunzmann, and Z. Zhang, "Quantization-aware and tensor-compressed training of transformers for natural language understanding," in *Proc. INTERSPEECH*, 2023, pp. 3292–3296.

[25] J. Xiao, C. Zhang, Y. Gong, M. Yin, Y. Sui, L. Xiang, D. Tao, and B. Yuan, "HALOC: Hardware-aware automatic low-rank compression for compact neural networks," in *Proceedings of the AAAI Conference on Artificial Intelligence*, vol. 37, no. 9, 2023, pp. 10 464–10 472.

[26] J. Gu, B. Keller, J. Kossaifi, A. Anandkumar, B. Khailany, and D. Z. Pan, "HEAT: Hardware-efficient automatic tensor decomposition for transformer compression," in *NeurIPS Workshop on Machine Learning for Systems*, 2022.

[27] J.-F. Zhang, C.-H. Lu, and Z. Zhang, "TetriX: Flexible architecture and optimal mapping for tensorized neural network processing," *IEEE Transactions on Computers*, vol. 73, no. 5, pp. 1219–1232, 2024.

[28] J. Lu, J. Tian, H. Li, I. Young, and Z. Zhang, "FETTA: Flexible and efficient hardware accelerator for tensorized neural network training," *arXiv preprint arXiv:2504.06474*, 2025.

[29] J. Tian, J. Lu, H. Li, X. Wang, C. C. Hao, I. Young, and Z. Zhang, "Ultra memory-efficient on-FPGA training of transformers via tensor-compressed optimization," *IEEE Transactions on Computer-Aided Design of Integrated Circuits and Systems*, 2025.

[30] Y. Chen, C. Hawkins, K. Zhang, Z. Zhang, and C. Hao, "3U-EdgeAI: Ultra-low memory training, ultra-low bitwidth quantization, and ultra-low latency acceleration," in *Proceedings of the Great Lakes Symposium on VLSI (GLSVLSI)*, 2021, pp. 157–162.

[31] H. T. Kung, "Why systolic architectures?" *Computer*, vol. 15, no. 1, pp. 37–46, 1982.

[32] Y.-H. Chen, J. Emer, and V. Sze, "Eyeriss: A spatial architecture for energy-efficient dataflow for convolutional neural networks," in *ACM/IEEE International Symposium on Computer Architecture (ISCA)*, 2016, pp. 367–379.

[33] N. P. Jouppi *et al.*, "In-datacenter performance analysis of a tensor processing unit," in *ACM/IEEE International Symposium on Computer Architecture (ISCA)*, 2017, pp. 1–12.

[34] A. Parashar, P. Raina, Y. S. Shao, Y.-H. Chen, V. A. Ying, A. Mukkara, R. Venkatesan, B. Khailany, S. W. Keckler, and J. Emer, "Timeloop: A systematic approach to DNN accelerator evaluation," in *IEEE International Symposium on Performance Analysis of Systems and Software (ISPASS)*, 2019, pp. 304–315.

[35] H. Kwon, P. Chatarasi, M. Pellauer, A. Parashar, V. Sarkar, and T. Krishna, "Understanding reuse, performance, and hardware cost of DNN dataflow: A data-centric approach," in *IEEE/ACM International Symposium on Microarchitecture (MICRO)*, 2019, pp. 754–768.

[36] R. Raj, S. Banerjee, N. Chandra, Z. Wan, J. Tong, A. Samajdar, and T. Krishna, "SCALE-Sim v3: A modular cycle-accurate systolic accelerator simulator for end-to-end system analysis," in *IEEE International Symposium on Performance Analysis of Systems and Software (ISPASS)*. IEEE, 2025, pp. 186–200.

[37] Y. Tang, X. Zhang, P. Zhou, and J. Hu, "EF-Train: Enable efficient on-device CNN training on FPGA through data reshaping for online adaptation or personalization," *ACM Transactions on Design Automation of Electronic Systems (TODAES)*, vol. 27, no. 5, pp. 1–36, 2022.

[38] C. Guo, B. Lou, X. Liu, D. Boland, P. H. Leong, and C. Zhuo, "BOOST: Block minifloat-based on-device CNN training accelerator with transfer learning," in *IEEE/ACM International Conference on Computer Aided Design (ICCAD)*. IEEE, 2023, pp. 1–9.

[39] D. G. A. Smith and J. Gray, "opt_einsum – a Python package for optimizing contraction order for einsum-like expressions," *Journal of Open Source Software*, vol. 3, no. 26, p. 753, 2018.